Intraventricular vector flow mapping—a Doppler-based regularized problem with automatic model selection

Kondo Claude Assi[1]**, Etienne Gay**[1]**, Christophe Chnafa**[2]**, Simon Mendez**[2]**, Franck Nicoud**[2]**, Juan F P J Abascal**[3]**, Pierre Lantelme**[3,4]**, François Tournoux**[1,5] **and Damien Garcia**[1,6]

[1] Research Center of the University of Montreal Hospital (CRCHUM), Montreal, QC, Canada
[2] University of Montpellier—IMAG CNRS UMR 5149, Montpellier, France
[3] CREATIS UMR 5220, U1206, University of Lyon, Villeurbanne, France
[4] Department of echocardiography, Croix-Rousse Hospital, Lyon, France
[5] Department of echocardiography, CHUM Hôtel-Dieu, Montreal, QC, Canada
[6] Faculty of medicine, Department of radiology, University of Montreal, Montreal, QC, Canada

E-mail: Garcia.Damien@gmail.com

Abstract

We propose a regularized least-squares method for reconstructing 2D velocity vector fields within the left ventricular cavity from single-view color Doppler echocardiographic images. Vector flow mapping is formulated as a quadratic optimization problem based on an ℓ_2-norm minimization of a cost function composed of a Doppler data-fidelity term and a regularizer. The latter contains three physically interpretable expressions related to 2D mass conservation, Dirichlet boundary conditions, and smoothness. A finite difference discretization of the continuous problem was adopted in a polar coordinate system, leading to a sparse symmetric positive-definite system. The three regularization parameters were determined automatically by analyzing the L-hypersurface, a generalization of the L-curve. The performance of the proposed method was numerically evaluated using (1) a synthetic flow composed of a mixture of divergence-free and curl-free flow fields and (2) simulated flow data from a patient-specific CFD (computational fluid dynamics) model of a human left heart. The numerical evaluations showed that the vector flow fields reconstructed from the Doppler components were in good agreement with the original velocities, with a relative error less than 20%. It was also demonstrated

that a perturbation of the domain contour has little effect on the rebuilt velocity fields. The capability of our intraventricular vector flow mapping (*i*VFM) algorithm was finally illustrated on *in vivo* echocardiographic color Doppler data acquired in patients. The vortex that forms during the rapid filling was clearly deciphered. This improved *i*VFM algorithm is expected to have a significant clinical impact in the assessment of diastolic function.

Keywords: ultrasound imaging, color Doppler, vector flow imaging, regularized least-squares, intracardiac flow imaging

S Supplementary material for this article is available online

(Some figures may appear in colour only in the online journal)

1. Introduction

During diastole, as blood flows from the left atrium to the left ventricle through the mitral aperture, a vortex ring is formed. This vortex, by rotating in the natural flow direction, redirects blood momentum toward the left ventricular outflow tract and facilitates flow transit to the aorta during ejection (Bermejo *et al* 2015). When the filling of the left ventricle is impaired (presence of diastolic dysfunction), a modification of the blood flow patterns can occur, with a significant impact on the vortices (Abe *et al* 2013). Concordantly, it has been reported that a strong physiological linkage exists between the volume of the vortex and that of the healthy heart, whereas this relationship is lost in patients with heart failure (Arvidsson *et al* 2016). Vortices are thus known to be distinct local flow imprints. In particular, the clinical importance of intraventricular vortex formation has been underlined by Pedrizzetti *et al* (2014). These clinically relevant flow patterns are accessible if the full velocity vector field is available (Sengupta *et al* 2012, Bermejo *et al* 2015). Cardiac magnetic resonance (CMR) and contrast-enhanced ultrasound are the most commonly used medical imaging modalities for analysis of the left intraventricular blood flow dynamics (Sengupta *et al* 2012). Velocity-encoding CMR requires multi-beat acquisition and retrospective temporal registration to retrieve the flow dynamics at a sufficient temporal resolution (Elbaz *et al* 2014). This approach cannot be used clinically because of its poor cost-effectiveness. By contrast, ultrasound vector flow imaging (Jensen *et al* 2016) has the advantage of being portable and inexpensive. Vector flow imaging by contrast-enhanced echocardiography (often called echo-PIV, echographic particle image velocimetry) is based on the tracking of speckles generated by contrast agents, which are perfused to raise the blood signal (Kim *et al* 2004, Abe *et al* 2013). Contrast-enhanced echo-PIV has been used in clinical research to analyze the dynamics of the vortices that arise in the left ventricular cavity (Abe *et al* 2013, Agati *et al* 2014). The major clinical limitation of echo-PIV is the intravenous administration of gas-filled microbubbles, which makes this procedure time- and staff-consuming. A recent study, however, showed that intracardiac blood speckle velocimetry is feasible in neonates without contrast agent (Fadnes *et al* 2014). Alternative ultrasound approaches based on color Doppler have also been reported to analyze the formation of the main vortex during early diastole (Garcia *et al* 2010, Mehregan *et al* 2014, Faurie *et al* 2017).

Doppler ultrasound is presently the clinical imaging modality of choice for evaluating blood flow within the heart cavities. The Doppler velocities represent the orthogonal projections of the actual velocity vectors onto the ultrasound scanlines, thus leading to incomplete 1D flow information. For this reason, cardiac color Doppler is generally used as a mere visualization tool in the clinical context. During the last decade, there has been an interest in reconstructing the

intracardiac velocity vector fields by postprocessing color-Doppler images. Arigovindan *et al* (2007) restored 2D velocity vector fields by combining two Doppler images acquired from different transthoracic acoustic windows. Gomez *et al* (2015) generalized this technique and proposed a 3D reconstruction of the flow vector fields using several volumetric color Doppler images. When combining Doppler images or volumes, the echocardiographic views must be significantly different to make the reconstruction problem well-posed. This can be a major constraint in a clinical situation since the number of acoustic windows for high-quality color Doppler is limited. In addition, accurate temporal and spatial registrations are required to match the color Doppler series acquired during successive heart beats. The first methods for a 2D vector reconstruction based on single-view color Doppler images were reported in Garcia *et al* (2010) and Uejima *et al* (2010). The *i*VFM (intraventricular vector flow mapping) method proposed by Garcia *et al* (2010) works in the polar coordinate system associated with an apical three-chamber scan sector (figure 1). It consists in computing the cross-beam (angular) velocity components from the Doppler (radial) velocities by integrating the 2D continuity equation across the scanlines. Garcia *et al*'s *i*VFM technique is now implemented in Hitachi ultrasound scanners (Tanaka *et al* 2015) and has been the routine tool in recent clinical studies to investigate the intraventricular flow patterns in cardiomyopathies (Nogami *et al* 2013, Ro *et al* 2014). This approach examines each angular line independently, which generates vector discontinuities along the radial direction. Incorrect apical alignments can also lead to significant inconsistencies. Furthermore, the current *i*VFM algorithm cannot be adapted for 3D color Doppler.

We therefore propose to generalize this Doppler-based algorithm using a regularized least-squares method with automatic selection of the regularizing parameters. We introduce a general 2D approach with the future perspective of adapting *i*VFM for volumetric color Doppler. The velocity field to be reconstructed was formulated as the minimizer of a cost function composed of a Doppler-based objective function and a regularizer containing physically motivated operators. A finite difference discretization of the continuous problem was adopted in a uniform polar grid, leading to an unconstrained quadratic optimization problem, which can be solved with efficient linear algebra algorithms. The performance of the improved *i*VFM technique was numerically evaluated using a patient-specific computational fluid dynamics (CFD) heart model. It was then clinically tested in several patients to disclose the vortex formation during filling.

2. Methods

2.1. The quadratic optimization problem for vector flow reconstruction

Figure 1 illustrates an annulus sector scan from 2D color Doppler echocardiography. We will work in a polar coordinate system $\{r, \theta\}$ whose pole is the center of the annulus sector. In transthoracic echocardiography, the successive ultrasound beams that form the image have a radial direction. Color Doppler provides the flow velocity projections parallel to the direction of the ultrasound beams. By convention, the Doppler velocities u_D are positive when the blood flows towards the ultrasound probe. Let $v_D = -u_D$ to ensure sign compatibility between v_D and the radial components v_r of the actual velocity field $\vec{v}$. Using this notation, color Doppler only provides the following information in a set of sampling points:

$$v_D(r, \theta) = \vec{v}(r, \theta) \cdot \vec{e}_r + \eta(r, \theta) \equiv v_r(r, \theta) + \eta(r, \theta), \tag{1}$$

where $\vec{e}_r$ is the unit radial vector and η is the Doppler noise. From this incomplete and noisy information, we wish to estimate the radial and angular components $\{v_r, v_\theta\}$ of the actual blood velocity field. Let Ω be the domain of interest, a closed region in the Doppler sector, with boundary $\partial\Omega$, and let $\{\boldsymbol{x}_i = [r_i, \theta_i], i = 1 \ldots K\}$ be the sampling points in Ω. The velocity field reconstruction problem can be phrased as follows:
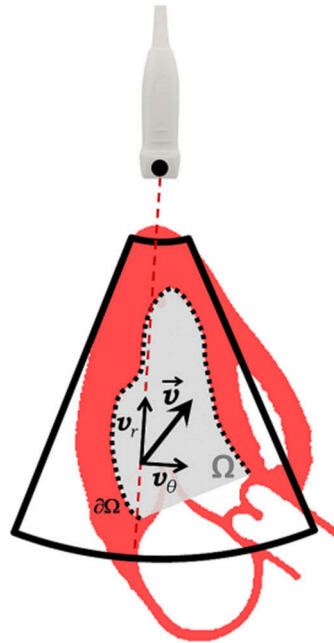
Figure 1. The *i*VFM algorithm was implemented in the polar coordinate system associated with the Doppler sector. *i*VFM allows one to recover the 2D velocity field $\vec{v}(r,\theta)$ from the Doppler components by minimizing the cost function described by equation (2). Ω represents the domain of interest and $\partial\Omega$ its boundary.

Given the Doppler measurements characterized by the set of triplets $\{(r_i, \theta_i, v_{D_i}), i = 1 \ldots K\}_\Omega$, compute the radial and angular components $\{(v_r, v_\theta)_i, i = 1 \ldots K\}_\Omega$ of the unknown velocity vector field $\vec{v}$ in the domain of interest.

In the global *i*VFM approach (figure 2 gives an overview), the velocity field estimation problem is rewritten as an unconstrained minimization problem: $\underset{\vec{v}}{\arg\min} \; J(\vec{v})$, where the cost function J is written as:

$$J(\vec{v}) = J_0(\vec{v}) + \lambda_1 J_1(\vec{v}) + \lambda_2 J_2(\vec{v}) + \lambda_3 J_3(\vec{v})$$

$$= \underbrace{\int_\Omega (v_r - v_D)^2}_{\substack{1)\ \text{fit to the} \\ \text{Doppler data}}} + \lambda_1 \underbrace{\int_\Omega (r\partial_r v_r + v_r + \partial_\theta v_\theta)^2}_{\substack{2)\ \text{null-divergence} \\ \text{constraint}}} + \lambda_2 \underbrace{\int_{\partial\Omega} \left(\vec{v} \cdot \vec{d}_{\text{wall}}\right)^2}_{\substack{3)\ \text{boundary} \\ \text{conditions}}} + \ldots$$

$$\lambda_3 \sum_{m \in \{r,\theta\}} \underbrace{\int_\Omega \left(r^2 \partial_r^2 v_m\right)^2 + 2\left(r\partial_{r\theta}^2 v_m\right)^2 + \left(\partial_\theta^2 v_m\right)^2}_{4)\ \text{smoothness constraint}}.$$

$$(2)$$

The regularization parameters $\lambda_l > 0, (l = 1, 2, 3)$ were selected automatically using an *L*-hypersurface, as explained in section 2.2.

(1) The first term J_0 in J is the objective function related to the Doppler data.
(2) The second term J_1 is associated with the 2D null-divergence assumption (Garcia *et al* 2010); $r \operatorname{div}(\vec{v}) = r\partial_r v_r + v_r + \partial_\theta v_\theta = 0$ is the expression of the mass conservation in
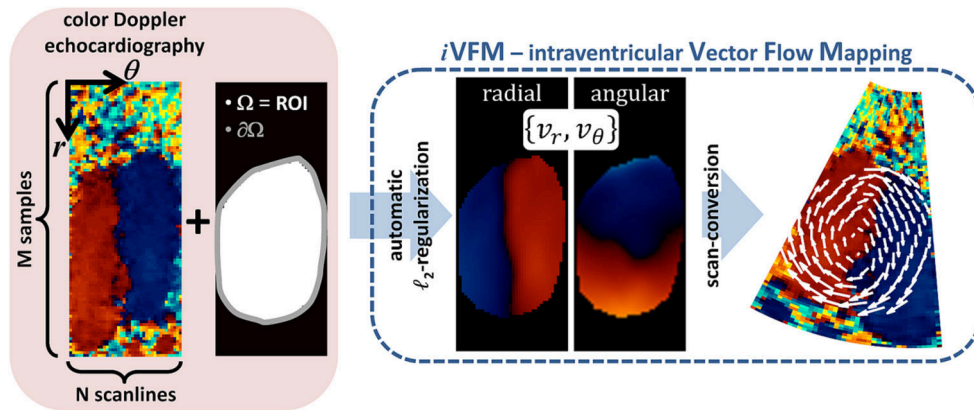
Figure 2. The *i*VFM algorithm is based on an automatic ℓ_2-norm minimization. It works in a polar coordinate system, before scan conversion. Ω represents the domain of interest and $\partial\Omega$ is its boundary.

polar coordinates assuming that the out-of-plane components are negligible. As shown in Garcia *et al* (2010), the 2D divergence-free assumption is acceptable on the plane corresponding to the three-chamber apical long-axis view.

(3) The third term J_2 is related to the boundary conditions on the endocardium (inner cardiac wall). The direction vector $\vec{d}_{\mathrm{wall}}$ is located on the wall boundary $\partial\Omega$ (the endocardium). As in Garcia *et al* (2010), we choose $\vec{d}_{\mathrm{wall}} = \vec{n}_{\mathrm{wall}}$, i.e. the wall direction vectors were equal to the unit normal vectors perpendicular to the boundary. In other words, it was assumed that the flow was parallel to the bounding surface in the immediate vicinity of the endo-cardial wall. Alternative boundary conditions could be imposed with this approach. Using $\vec{d}_{\mathrm{wall}} = \vec{t}_{\mathrm{wall}}$ (unit tangential vector) would favor flow perpendicularity to the bounding surface. If the radial and angular components of the wall velocities are known, equaling $\vec{d}_{\mathrm{wall}}$ to $[-v_{\theta,\mathrm{wall}}, \ v_{r,\mathrm{wall}}]$ can approximate a no-slip condition.

(4) The last term J_3 is associated with some desirable smoothness properties of the velocity field. The actual blood flow velocity, at a specific location and instant in the cardiac cycle, fluctuates around an expected value. In the physiological hemodynamic situations, leaving aside the flow fluctuations (Chnafa *et al* 2016), the expected mean velocity field varies smoothly in both time and space. To impose spatial smoothness in the expected velocity field, we used second-order partial derivatives with cross terms.

An approximate solution of the minimization problem was computed over a polar grid with constant radial and angular steps (h_r and h_θ). The differential operators in the cost function (2) were replaced by their discrete counterpart using three-point stencils. Using ℓ_2-norms, the corresponding discretized scheme reduced to an unconstrained quadratic problem, as shown below. For the sake of a compact matrix formulation, we introduce the following matrices, all of size $(M \times N)$, where N is the number of scanlines and M the number of samples per scanline (figure 2):

- $\boldsymbol{V_D}$ contains the negative Doppler velocities. It is obtained by taking the negative of the Doppler image returned by the scanner before scan conversion.
- $\boldsymbol{V_r}$ and $\boldsymbol{V_\theta}$ contain the radial and angular velocities to be estimated.
- $\boldsymbol{R}$ contains the radial coordinates of the grid nodes.

- N_r and N_θ contain the radial and angular components of the unit vector normal to the cardiac inner wall (endocardium), respectively. $(N_r)_{k,l}$ and $(N_\theta)_{k,l} = 0$ if the element (k,l) is not on the endocardium.

We work with the elements inside and on the edge of the region defined by the left ventricular cavity. This region is defined by the binary matrix $\mathbf{\Delta}$, with $(\mathbf{\Delta})_{k,l} = 1$ if the element (k,l) is inside or on the edge of the region of interest (ROI), $(\mathbf{\Delta})_{k,l} = 0$ otherwise.

We also define the following column vectors of size $(MN \times 1)$ obtained by vectorizing the above-mentioned matrices:

$$v_D = \text{vec}\,(V_D)\,,\ v_r = \text{vec}\,(V_r)\,,\ v_\theta = \text{vec}\,(V_\theta)\,,\ r = \text{vec}\,(R)\,,\ n_r = \text{vec}\,(N_r)\,,\ n_\theta = \text{vec}\,(N_\theta)\ \text{and}\ \delta = \text{vec}\,(\mathbf{\Delta})\,.$$

I_q refers to the identity matrix of size $(q \times q)$, and $\mathbb{I}_q$ to a column vector of ones of size $(q \times 1)$, where q is a general length. The Hadamard (entrywise) and Kronecker products are noted $\circ$ and $\otimes$. The entrywise square is noted $r^{\circ 2} = r \circ r$. The first- and second-order derivative operator matrices of size $(q \times q)$ are based on a three-point stencil; they are noted $\dot{D}_q$ and $\ddot{D}_q$. We finally note $v = \begin{bmatrix} v_r^{\text{T}} & v_\theta^{\text{T}} \end{bmatrix}^{\text{T}}$ the column vector of size $(2MN \times 1)$, solution of the minimization problem. The mathematical derivation of the linear system is extensively described in the supplemental content (stacks.iop.org/PMB/62/7131/mmedia). Using the above-mentioned notations, it follows that the discretized cost function can be written as:

$$J\,(v) = (Q_0 v - v_D)^{\text{T}} \,(Q_0 v - v_D) + \sum_{l=1...3} \lambda_l\, v^{\text{T}} Q_l^{\text{T}} Q_l v, \tag{3}$$

where Q_0, Q_1, Q_2 are three sparse matrices of size $(MN \times 2MN)$, and Q_3 is a sparse matrix of size $(6MN \times 2MN)$. They are given by (see the supplemental content):

$$Q_0 = [1\ \ 0] \otimes I_{MN};$$

$$Q_1 = \left[\frac{1}{h_r} \left(r\,\mathbb{I}_{MN}^{\text{T}} \right) \circ \left(I_N \otimes \dot{D}_M \right) + I_{MN}, \quad \frac{1}{h_\theta} \dot{D}_N \otimes I_M \right];$$

$$Q_2 = \left[\text{diag}\,(n_r), \quad \text{diag}\,(n_\theta) \right];$$

$$Q_3 = \begin{bmatrix} I_2 \otimes \frac{1}{h_r^2} \left(\left(r^{\circ 2}\,\mathbb{I}_{MN}^{\text{T}} \right) \circ \left(I_N \otimes \ddot{D}_M \right) \right) \\ I_2 \otimes \frac{2}{h_r h_\theta} \left(\left(r\,\mathbb{I}_{MN}^{\text{T}} \right) \circ \left(\dot{D}_N \otimes \dot{D}_M \right) \right) \\ I_2 \otimes \frac{1}{h_\theta^2} \left(\ddot{D}_N \otimes I_M \right) \end{bmatrix}. \tag{4}$$

The operator diag denotes the diagonal matrix. Minimizing the cost function $J\,(v)$ (equations (3) and (4)) leads to the following linear system:

$$Av = b, \quad \text{with}$$

$$A = Q_0^{\text{T}} Q_0 + \sum_{l=1...3} \lambda_l Q_l^{\text{T}} Q_l = \begin{bmatrix} 1 & 0 \\ 0 & 0 \end{bmatrix} \otimes I_{MN} + \sum_{l=1...3} \lambda_l\, Q_l^{\text{T}} Q_l.$$

$$\text{and } b = Q_0^{\text{T}} v_D = \begin{bmatrix} 1 \\ 0 \end{bmatrix} \otimes v_D. \tag{5}$$

The matrix A is sparse symmetric and of size $(2MN \times 2MN)$, and b is a column vector of size $(2MN \times 1)$. From its expression, and because the scalars λ_l are positive, A is also positive semi-definite. The positive definiteness of A is guaranteed if Q_2 is defined appropriately, i.e. if the chosen boundary conditions make A nonsingular. Furthermore, the λ_l must be sufficiently large to ensure that the problem is well-conditioned. The sparse linear system (5) can be efficiently solved using the Cholesky decomposition. In practice, because we are working only with the elements inside or on the edge of the ROI, Q_0 and b must be rewritten as:

$$\boldsymbol{Q}_0 = [1\,0] \otimes \mathrm{diag}\left(\boldsymbol{\delta}\right) \text{ and } \boldsymbol{b} = \begin{bmatrix} 1 \\ 0 \end{bmatrix} \otimes \left(\mathrm{diag}\left(\boldsymbol{\delta}\right) \boldsymbol{v_D}\right). \tag{6}$$

2.2. Automatic parameter selection

The proposed *i*VFM velocity vector field reconstruction leads to a multi-parameter regularized problem. The approaches usually used for automatic parameter selection are the generalized cross-validation (Craven and Wahba 1978) and the *L*-curve (Hansen and O'Leary 1993), which are well suited for a single regularization parameter. Here we propose a method for selecting the regularization parameter triplet $\Lambda = (\lambda_1, \lambda_2, \lambda_3)$ of the *i*VFM problem. The *L*-curve method (Hansen and O'Leary, 1993) is one of the well-known approaches for the selection of a single regularization parameter. It allows one to find an optimal trade-off between the amount of regularization and the quality of the fitting to the given data. The *L*-curve (so-called due to its typical shape) consists in a log-log plot of the residual norm versus the regularization norm for a set of regularization parameter values. By defining the corner to be the point on the *L*-curve where the curvature reaches a maximum, an appropriate regularization parameter Λ_{opt} is chosen in such a way that the corresponding point lies on this corner (Hansen 2000). The *L*-hypersurface approach has been introduced to extend the *L*-curve method to multi-parameter regularization problems (Belge *et al* 2002). Let us introduce the residual norm:

$$\zeta\left(\Lambda\right) = \|\boldsymbol{v_D} - \boldsymbol{Q}_0 \boldsymbol{v}\left(\Lambda\right)\|^2, \tag{7}$$

and the regularization norms:

$$\chi_l\left(\Lambda\right) = \|\boldsymbol{Q}_l \boldsymbol{v}\left(\Lambda\right)\|^2, \, l = 1, 2, 3. \tag{8}$$

where $\boldsymbol{v}\left(\Lambda\right)$ is the solution of the regularized problem (5) for a given $\Lambda\left(\Lambda \in \mathbb{R}_+^{*3}\right)$. The matrices $\boldsymbol{Q}_l \ (l = 1, 2, 3)$ are the regularization matrices defined earlier (equation (4)). Then the *L*-hypersurface is the three-surface in the hyperspace of four dimensions associated with the map $\mathcal{S}\left(\Lambda\right) : \mathbb{R}_+^{*3} \to \mathbb{R}^4$, such that (Belge *et al* 2002):

$$\mathcal{S}\left(\Lambda\right) = \left(\log\left(\chi_1\left(\Lambda\right)\right), \log\left(\chi_2\left(\Lambda\right)\right), \log\left(\chi_3\left(\Lambda\right)\right), \log\left(\zeta\left(\Lambda\right)\right)\right). \tag{9}$$

Similar to the *L*-curve, the *L*-hypersurface is a log-log plot of the residual norm $\zeta\left(\Lambda\right)$ against the regularization norms $\chi_l\left(\Lambda\right)$, $l = 1, 2, 3$. To deal with the *L*-hypersurface-based parameter selection, one may consider the generalized corner point, where a balance between the regularization and residual errors is expected (Belge *et al* 2002). To identify the corner point corresponding to the optimal solution $\boldsymbol{v}\left(\Lambda_{\mathrm{opt}}\right)$, we proceeded by iterating as follows:

(1) Provide an initial Λ; $i = 0$.
(2) For the fixed pair $\left(\lambda_{1+[i(\mathrm{mod}3)]}, \lambda_{1+[(i+1)(\mathrm{mod}3)]}\right)$, find the corner point of the discrete *L*-curve with respect to $\lambda_l = \lambda_{1+[(i+2)(\mathrm{mod}3)]}$ and associated with the map $\mathcal{S}_l\left(\lambda_l\right) = \left(\log\left(\chi_l\left(\lambda_l\right)\right), \log\left(\zeta\left(\lambda_l\right)\right)\right)$. Note that mod stands for modulo.
(3) Update Λ using the current estimate λ_l.
(4) Check convergence of Λ.
(5) If necessary, increment i and go to step #2, i.e. iterate periodically among two combinations of Λ.

This iterative method allowed automatic model selection. This is an essential aspect in the clinical context, since it avoids subjectivity in the choice of the parameters, and consequently notably reduces interobserver variability. Using a Λ step tolerance of 0.1 in a decimal logarithmic scale, around ten iterations were required with the patient data reported in section 3.3.
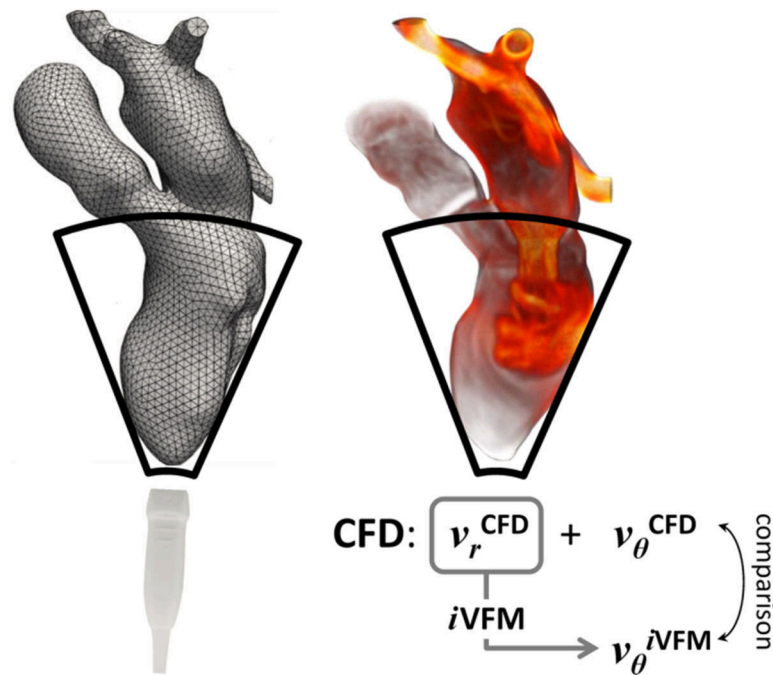
Figure 3. The *i*VFM algorithm was tested in a dynamic patient-specific heart flow model (Chnafa *et al* 2014). Doppler velocity images were simulated from the radial velocity components. The vector fields recovered by *i*VFM were compared with the ground-truth CFD fields.

2.3. Analysis in a rigid-body vortex model

The *i*VFM algorithm was first tested in a numerical rigid-body vortex model. The purpose of these simulations was to analyze the robustness of the algorithm to hypothesis failures, i.e. under conditions where (1) the actual flow is not divergence-free or (2) the imposed boundary conditions in J_2 are incorrect. The diameter of the vortex was 8 cm, and its center was located 6 cm from the ultrasound probe. Synthetic 90°-wide Doppler images were generated by extracting the radial velocity components. They contained 64 scanlines, with 100 samples per scanline. The Doppler velocities were corrupted by a zero-mean Gaussian white noise with a velocity-dependent local variance (Jensen 1996). Signal-to-noise ratios were within the range (20, 60) dB (see equations (10) and (11) in Muth *et al* (2011)). In a first series of simulations, to test the algorithm in non-divergence-free flows, the rigid vortex (divergence-free, uniform curl) was mixed with a uniform sink flow (uniform divergence, curl-free) with an identical flow rate, according to the following weighted sum: $(1 - p)$ vortex $+ p$ sink, $p \in [0, 0.25]$ ($p = 0$ indicates a true divergence-free hypothesis). To test the effect of incorrect boundary conditions, a second series of rigid-body vortices was examined while imposing different boundary conditions in J_2. In this series, the direction wall vector was defined by $\vec{d}_{\text{wall}} = (1 - p) \, \vec{n}_{\text{wall}} + p \, \vec{t}_{\text{wall}}, p \in [0, 0.25]$ ($p = 0$ indicates true boundary conditions). The reconstructed velocity fields were compared with the actual fields for the two series. The root-mean-square errors were normalized by the maximum speed:

$$nRMSE = \frac{1}{\max\|\vec{v}_{\text{actual}}\|} \sqrt{\frac{1}{n}\sum_{i=1}^{n}\|\vec{v}_{\text{estimated}_i} - \vec{v}_{\text{actual}_i}\|^2}. \tag{10}$$

2.4. Analysis in a patient-specific CFD heart model

To test the new *i*VFM algorithm under physiological-like conditions, we used a patient-specific heart flow CFD model developed by Chnafa *et al* (2014, 2015, 2016). In this CFD model, the cardiac cavities and the wall dynamics were extracted from 4D images acquired by computed tomography (figure 3). An arbitrary Lagrangian–Eulerian (ALE) framework was adopted to handle the large-amplitude motion of the cardiac tissues (endocardium and valve leaflets). Several complete intracardiac flow cycles were simulated in the left heart (details in Chnafa *et al* (2014, 2015)). Color Doppler velocity data were simulated from the phase-averaged intraventricular CFD flow velocities. An apical three-chamber view was reproduced (figure 3) by locating the probe at the apex, with the Doppler sector enclosing the mitral inlet and the left ventricular outflow tract. The virtual Doppler images were obtained in an evenly spaced polar grid (64 scanlines, 100 samples/scanline) by extracting the radial velocity components. A 60 dB signal-to-noise ratio was simulated. No clutter was included. Tangent-velocity boundary conditions (i.e. $\vec{d}_{\text{wall}} = \vec{n}_{\text{wall}}$, equation (2)) were assumed in the *i*VFM computation. The *i*VFM-derived velocities were compared with the original CFD velocities along the apex-mitral scanline. The root-mean-square errors were normalized by the maximum speed (equation (10)). The peak vorticities were also compared during diastole. To quantify the dependence of the *i*VFM reconstruction accuracy upon the left ventricular wall geometry, additional numerical experiments were conducted with disturbed walls. The idea was to mimic variations in the boundary wall delineation that occur from one operator to another in the clinical context. For a given frame, several wall geometries were considered. The perturbation was quantified using the Hausdorff distance between the actual endocardium boundary and the disturbed wall.

2.5. Analysis in patients

The new *i*VFM technique was tested retrospectively in several patients (no valvular regurgitation, no arrhythmia) with good-quality B-mode/color Doppler, to highlight the intraventricular blood flow and the vortex formation. Echo-Doppler images of the left ventricular inflow were acquired in the apical long-axis three-chamber view using a Vivid e9 ultrasound scanner (GE Healthcare) and a 2.5 MHz phased array. Doppler data were extracted prior to scan conversion (i.e. in a polar grid) using EchoPAC (GE Healthcare). The Doppler velocities were dealiased using the segmentation-based technique described in Muth *et al* (2011), and the inner left ventricular boundary was segmented manually. The protocol was approved by the human ethics review committee of the CHUM (Centre Hospitalier de l'Université de Montréal).

3. Results

3.1. Rigid-body vortex model

The *i*VFM algorithm lost some accuracy when the ideal conditions (i.e. divergence-free flow and exactness of the boundary conditions) were not met (figure 4). A normalized error

higher than 10% was observed when the hypotheses failed at >20% (parameter $p > 0.2$). The Doppler noise had a relatively small impact in comparison with the effect of the hypothesis breaches.

3.2. Analysis in the patient-specific CFD heart model

Figure 5 (top row) shows examples of *i*VFM-velocity fields compared with the CFD vector fields (bottom row). A qualitative inspection of the results shows that the reconstructed velocity field was in good agreement with the actual vector field. A quantitative error analysis is shown in figure 6. The normalized root-mean-square errors (on the long axis) reached maxima during left ventricular filling, when the velocities were the largest. Overall, the errors were less than 5% and 15% for the radial and angular velocities, respectively. The peak vorticities were also in good agreement, although the *i*VFM reconstruction induced some underestimation (maximum = 130 versus $160 \, \mathrm{s}^{-1}$). Although a small increase in angular error can be noted (figure 7), wall perturbation (in the range 0–12 mm) had no significant effect on velocity reconstruction, which illustrates the robustness of *i*VFM to potential errors in wall delineation.

3.3. Vector flow mapping in patients

The vector flow maps returned by the *i*VFM algorithm made the intraventricular flow patterns clearly discernible. The vortex formation, and its evolution over diastole, can be appreciated in figure 8. In this figure, the main vortex was detected and highlighted using the Okubo–Weiss criterion (Weiss 1991). Figure 9 provides diastolic snapshots in three additional patients, revealing the large vortex that forms in the cardiac cavity.

4. Discussion

We have introduced a regularized approach to reconstruct the 2D intraventricular velocity vector field from single-view color-Doppler echocardiography images. This method extends the one reported in Garcia *et al* (2010) and Hendabadi *et al* (2013). Unlike the previous work that solved a series of 1D continuity equations independently, the present *i*VFM solves a linear system derived from the discretization of a 2D cost function defined on the three-chamber intracavitary plane. This 2D numerical derivation will form the framework of an upcoming procedure for 3D vector flow mapping using single-window Doppler echocardiography, as discussed in section 4.5.

4.1. Quality of the reconstructed vector maps

The quality of the flow restoration appears to be related to the frame in the cardiac cycle. In some instants of the cardiac cycle, the intraventricular flow is mostly radial (parallel to the ultrasound beam direction), and as such is 'easily' reconstructible. In some other parts of the cardiac cycle, when a large vortex is formed (as in figure 9), the vector flow field contains substantial cross-beam (angular) components. This explains why errors are higher at some point in time. In a planar imaging modality, divergence minimization alone cannot allow the full recovery of the actual vector field since significant out-of-plane velocity components can exist. The observed errors (less than 15–20%), however, are acceptable in a clinical context. Whether the reconstruction errors remain satisfactory in patients must be confirmed by comparing *i*VFM against a true 2D imaging technique, such as echo-PIV by
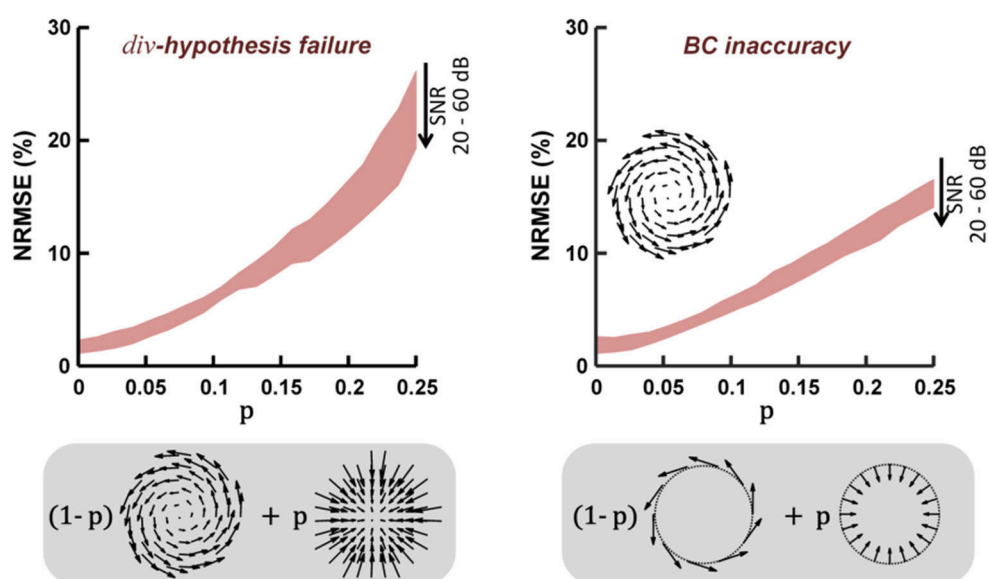
Figure 4. Analysis in the synthetic rigid vortex: the *i*VFM cost function includes a 'divergence-free' regularizer. The left panel shows the effect of the divergence-hypothesis breach on *i*VFM accuracy. The synthetic flow is divergence-free when $p = 0$. The right panel shows the impact of BC (boundary condition) imprecision. The boundary conditions are exact when $p = 0$. Doppler noise (signal-to-noise ratio = 20–60 dB) has relatively little effect on *i*VFM accuracy. The inset represents the rigid vortex.

contrast echocardiography (Abe *et al* 2013) or flow MRI (Markl *et al* 2016). Although the endocardium geometry is known to have an impact on the intraventricular flow, we showed clear evidence that small perturbations of the wall do not affect the reconstructed fields significantly. According to these results, the *i*VFM algorithm is more sensitive to non-divergence-free flows and erroneous boundary conditions than to variations in wall geometry.

4.2. Expected reproducibility in clinical applications

Recovering flow vector fields in the left ventricle is a required step to fully characterize the principal vortex that forms during diastole. According to recent clinical studies, this vortex might provide valuable echocardiographic markers for the assessment of diastolic dysfunction (Abe *et al* 2013, Arvidsson *et al* 2016). If the clinical relevance of vortex properties for diastology is confirmed by further prospective studies, vortex imaging by *i*VFM must be fast and reproducible to become an accepted echocardiographic procedure. Fastness is ensured since *i*VFM only requires a single color Doppler cineloop; furthermore, solving the sparse linear system with automatic model selection was a less-than-1 s operation. To guarantee interobserver reproducibility, a necessary condition is the automatic selection of the three regularization parameters to avoid any subjectivity. The multi-view methods proposed in Arigovindan *et al* (2007) and Gomez *et al* (2015), discussed in section 4.3, do not explicitly give details on the method used for optimal parameter selection. Methods for automatic parameter selection, such as the generalized cross-validation and the *L*-curve have been used for regularization problems, mainly with a single regularization parameter. The *L*-hypersurface was reintroduced by Belge *et al* (2002) to handle multiple parameters. These authors first proposed an approach based on the maximization of the Gaussian curvature of the *L*-hypersurface (Belge *et al* 1998). They
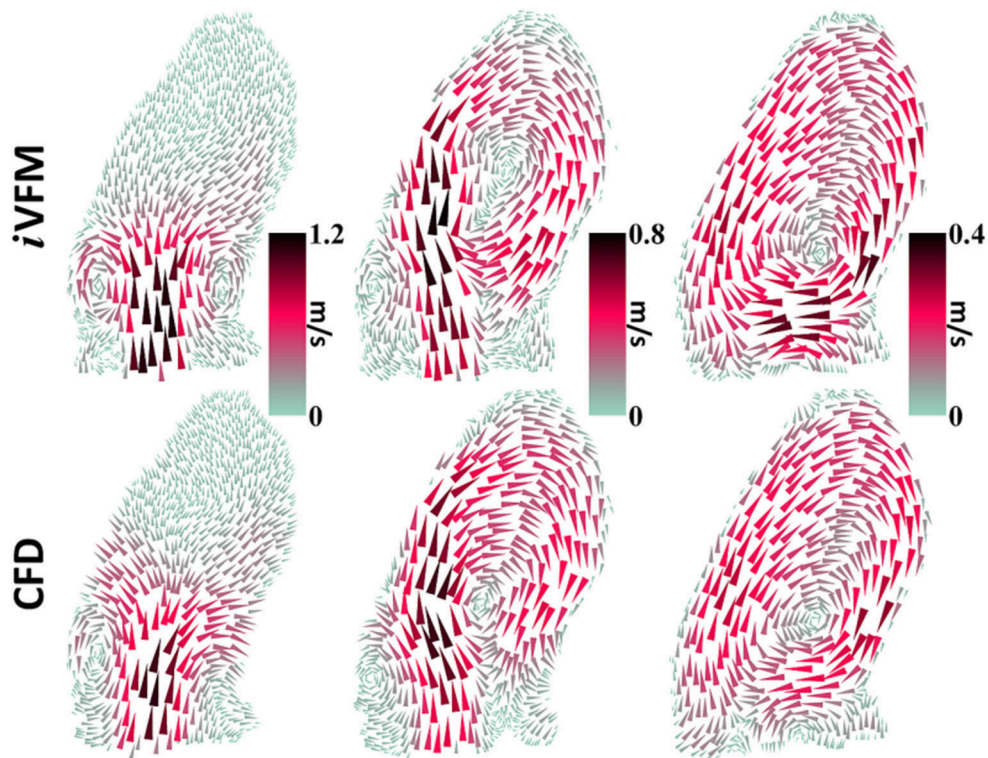
Figure 5. Analysis in the patient-specific CFD heart model: comparison of the intraventricular velocity vector fields (*i*VFM-based vectors versus original CFD vectors). These snapshots correspond to frame numbers 50, 60, and 70 (see figure 6).
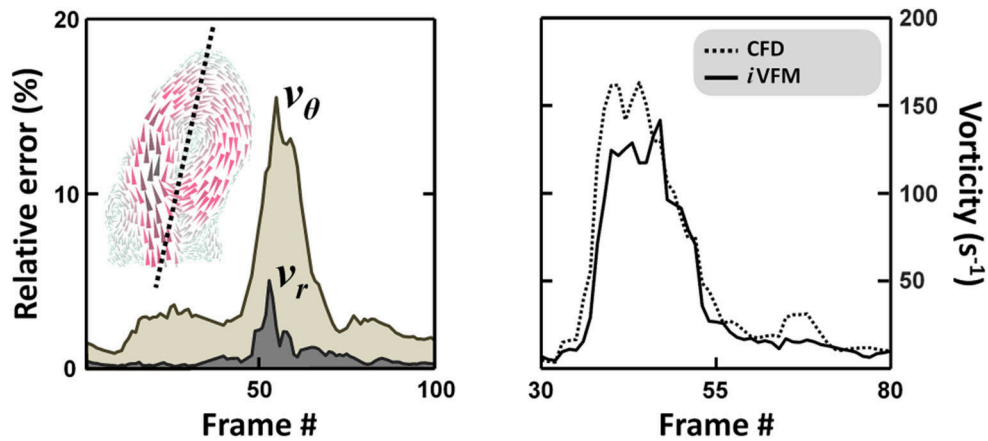

Figure 6. Analysis in the patient-specific CFD heart model. Left panel: comparison between the *i*VFM-based and CFD velocity vectors. The radial and angular components were compared on the apex-mitral axis (dotted line of the inset). Right panel: comparison of the peak vorticities.
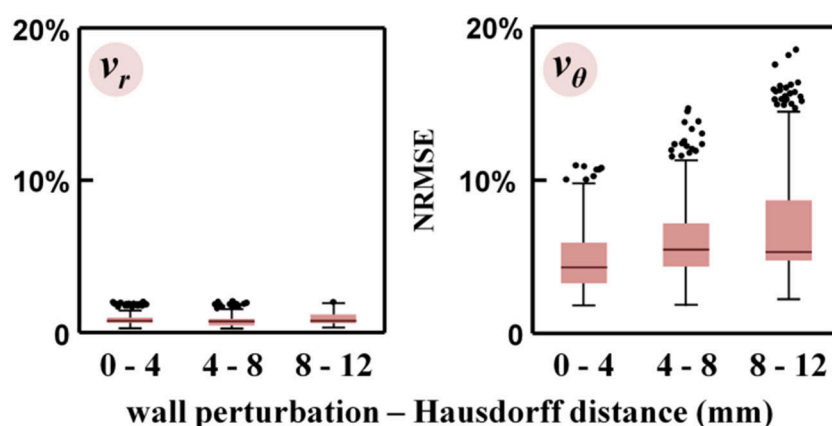
Figure 7. Analysis in the patient-specific CFD heart model. Impact of wall perturbation on *i*VFM accuracy. The radial and angular components were compared on the region of interest.

subsequently minimized a distance function to locate the *L*-hypersurface corner (Belge *et al* 2002). For these two cases, the whole hypersurface was considered. However, the complexity of the associated computations may justify considering other alternatives for dealing with the *L*-hypersurface (in our case, a 3D surface). In the present study, we considered the *L*-curve-like 1D slices iteratively, thus reducing the multi-parameter selection to a series of single-parameter determination. Convergence towards a unique solution is ensured if the *L*-hypersurface is strictly convex in the domain of interest. Although proving the convexity of the *L*-hypersurface is not within our expertise, convergence was always attained in our *in silico* and *in vivo* tests. The reproducibility of *i*VFM will be analyzed in a further clinical study.

4.3. Boundary conditions and well-posedness of the problem

The key constraint in the *i*VFM cost function (equation (2)) is the null-divergence constraint; it allows the estimation of the cross-beam velocity components under the assumption that fluid mass is 'approximately' conserved in the plane of interest. This assumption is acceptable in the echocardiographic three-chamber apical long-axis view (Garcia *et al* 2010). It should be noted that this assumption is formulated in a least-squares sense. As a consequence, the vector field reconstructed by *i*VFM is not necessarily divergence-free. The output also depends on the boundary conditions. Since the continuity equation is a partial differential equation, boundary conditions are required to uniquely define the problem. No-slip boundary conditions should be theoretically preferred, i.e. the same velocity for the fluid and the wall should be prescribed at the interface, because blood is a viscous fluid. However, as in the previous study (Garcia *et al* 2010), we favored (in a least-squares sense) blood velocities tangent to the endocardium since the intraventricular flow is highly inertial. Flow-MRI and CFD studies confirm that this condition is legitimate during diastole. Adequate boundary conditions guarantee the well-posedness of the problem. Indeed, the matrix A of the linear system is positive semi-definite; the quadratic function (3) is thus convex. If the Dirichlet boundary conditions on the endocardium are complete, the minimization problem is well-posed, thus ensuring strict convexity of the quadratic function (A is positive definite) and in turn the presence of a single minimizer. Our *in vitro* and *in vivo* numerical evaluations also showed that the system was well-conditioned, and thus the solutions were only slight (or not) sensitive to round-off errors.
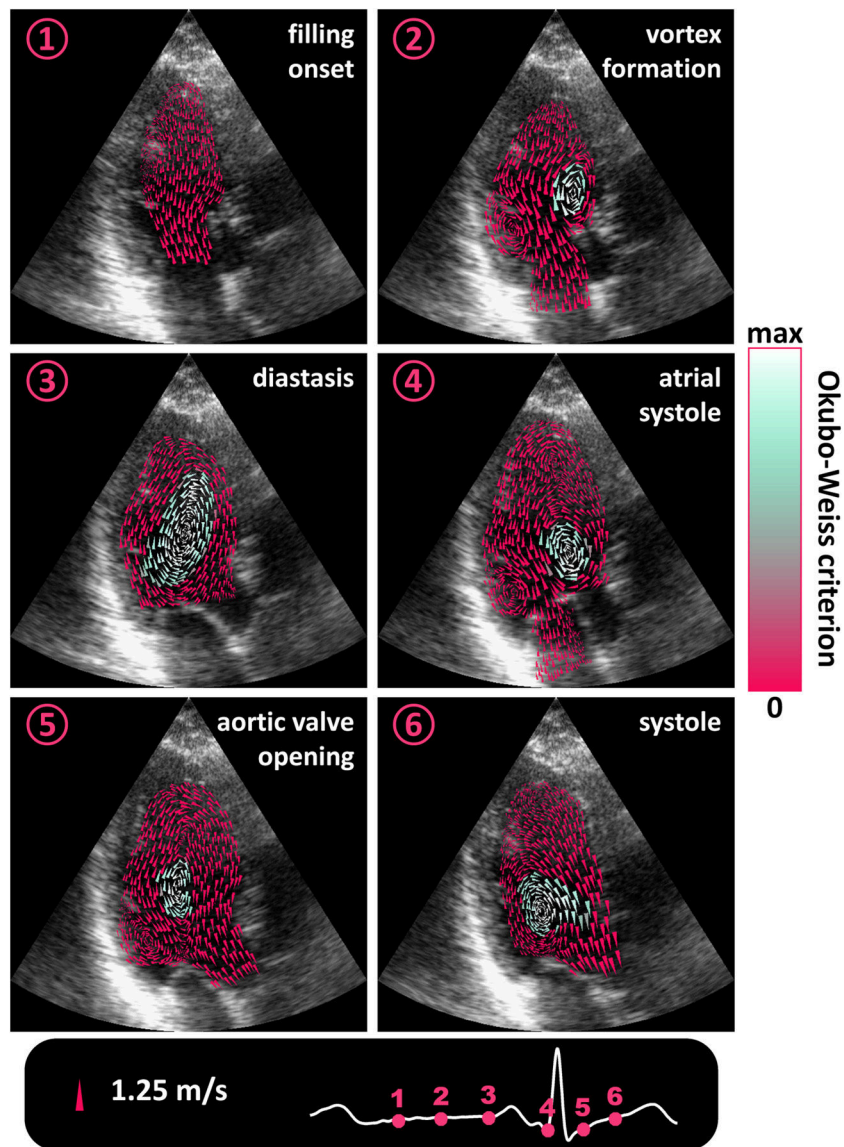
Figure 8. *i*VFM in a patient, from early filling to systole onset (see ECG). The vortices were detected by the Okubo–Weiss criterion. Only the main clockwise vortex is depicted.

4.4. Comparison with other color Doppler approaches

Several methods for intracardiac vector flow imaging using color Doppler echocardiography have been derived. The multiple-view approaches mentioned in the introduction require registration of several echocardiographic views acquired at significantly different beam angles, which hinders their clinical application. To make intraventricular vector flow imaging compatible with conventional color Doppler, reconstructions based on single-view images have been proposed. One advantage is that it can fit the clinical acquisition protocol of an echocardiography laboratory; one drawback is the loss of flow information. Different
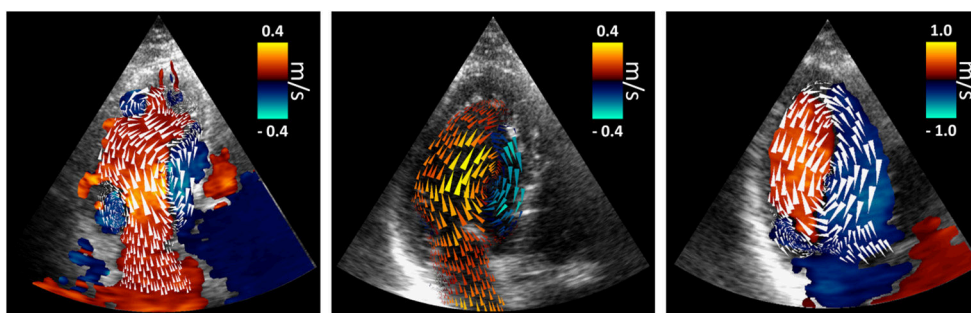
Figure 9. Diastolic intraventricular vortex in three patients, as depicted by *i*VFM. The red/blue colors represent the original Doppler velocities from which vector flow mapping was reconstructed.

models have been proposed to regularize the reconstruction problem. Four published studies are worth mentioning.

(1) Uejima *et al* (2010) broke down the intraventricular flow into a 'base' flow and a divergence-free axisymmetric vortical flow. This constraint can be acceptable with circular swirling flows, as used in Uejima *et al* (2010), but is in general not realistic under physiological conditions (see the elongated swirling flows in figure 9).

(2) Garcia *et al* (2010) integrated the 2D continuity equation across the scanlines in the leftward and rightward directions. A version of this algorithm is implemented in Hitachi ultrasound scanners (Tanaka *et al* 2015). If the output field is not properly post-processed, discontinuities may appear in the radial direction, as visible in the Hitachi scanner (e.g. see figure 6 in Ro *et al* (2014)).

(3) Pedrizzetti and Tonti (2012) wrote the velocity vector field as the sum of the Doppler field and an irrotational velocity field. The curl of the output field is therefore equal to that of the Doppler velocity field. This approach has no clear physical justification and can lead to severe underestimation of the vorticity amplitude.

(4) Jang *et al* (2015) claimed that they settled the 2D assumption dilemma by introducing an unknown source term in the 2D Navier–Stokes equation. Their argument is theoretically erroneous, resulting in a linear system with a singular matrix. The authors thus solved their ill-posed problem using a Tikhonov regularization, which added nonphysical constraints.

This series illustrates that any attempt to recover the actual intraventricular vector velocity field from a single 2D color Doppler view would be futile. Only an estimate can be retrieved because key information is missing. To obtain a 'good' estimate, the assumptions must have well-founded or reasonable physical meanings. Although our *in vivo* vector flow maps look physiologically consistent, a head-to-head comparison in patients with another vector imaging modality must still be carried out. Echo-PIV with contrast agents would be the method of choice since it would be uncomplicated to acquire similar echocardiographic fields of view.

4.5. 3D iVFM

The *i*VFM algorithm described in this study can be translated to 3D echocardiography. To this end, the cost function (2) must be rewritten with the three velocity components in a spherical coordinate system. Even if two components are unknown (both the polar and azimuthal components), instead of one, the problem will remain well-posed since the flow is divergence-free, and boundary conditions can be imposed on the surface of a closed volume. This will ensure

the strict convexity of the discretized cost function and thus the uniqueness of the minimizer. We expect volumetric *i*VFM to be more accurate than 2D *i*VFM since the divergence-free hypothesis is fully valid in 3D. Volumetric color Doppler, however, still suffers from low spatial and temporal resolutions. 3D *i*VFM will thus benefit from high-frame-rate color Doppler echocardiography (Provost *et al* 2014, Porée *et al* 2016, Posada *et al* 2016).

5. Conclusion

We have introduced an improved *i*VFM algorithm for *i*VFM using color Doppler echocardiography. This algorithm is based on a 2D minimization approach with physically consistent regularizers. It will form the framework for volumetric *i*VFM. This 2D *i*VFM method will be clinically relevant for assessing diastolic function in patients.

ORCID iDs

Simon Mendez ⬤ https://orcid.org/0000-0002-0863-2024
Damien Garcia ⬤ https://orcid.org/0000-0002-8552-1475

References

Abe H, Caracciolo G, Kheradvar A, Pedrizzetti G, Khandheria B K, Narula J and Sengupta P P 2013 Contrast echocardiography for assessing left ventricular vortex strength in heart failure: a prospective cohort study *Eur. Heart J.* **14** 1049–60

Agati L, Cimino S, Tonti G, Cicogna F, Petronilli V, De Luca L, Iacoboni C and Pedrizzetti G 2014 Quantitative analysis of intraventricular blood flow dynamics by echocardiographic particle image velocimetry in patients with acute myocardial infarction at different stages of left ventricular dysfunction *Eur. Heart J. Cardiovasc. Imaging* **15** 1203–12

Arigovindan M, Suhling M, Jansen C, Hunziker P and Unser M 2007 Full motion and flow field recovery from echo Doppler data *IEEE Trans. Med. Imaging* **26** 31–45

Arvidsson P M, Kovács S J, Töger J, Borgquist R, Heiberg E, Carlsson M and Arheden H 2016 Vortex ring behavior provides the epigenetic blueprint for the human heart *Sci. Rep.* **6** 22021

Belge M, Kilmer M E and Miller E L 1998 Simultaneous multiple regularization parameter selection by means of the L-hypersurface with applications to linear inverse problems posed in the wavelet transform domain *Proc. SPIE* **3459** 328–36

Belge M, Kilmer M E and Miller E L 2002 Efficient determination of multiple regularization parameters in a generalized L-curve framework *Inverse Problems* **18** 1161

Bermejo J, Martínez-Legazpi P and del Álamo J C 2015 The clinical assessment of intraventricular flows *Annu. Rev. Fluid Mech.* **47** 315–42

Chnafa C, Mendez S, Moreno R and Nicoud F 2015 Using image-based CFD to investigate the intracardiac turbulence *Modeling the Heart and the Circulatory System, MS&A* ed A Quarteroni (Berlin: Springer) pp 97–117

Chnafa C, Mendez S and Nicoud F 2014 Image-based large-eddy simulation in a realistic left heart *Comput. Fluids* **94** 173–87

Chnafa C, Mendez S and Nicoud F 2016 Image-based simulations show important flow fluctuations in a normal left ventricle: what could be the implications? *Ann. Biomed. Eng.* **44** 3346–58

Craven P and Wahba G 1978 Smoothing noisy data with spline functions. Estimating the correct degree of smoothing by the method of generalized cross-validation *Numer. Math.* **31** 377–403

Elbaz M S M, Calkoen E E, Westenberg J J M, Lelieveldt B P F, Roest A A W and van der Geest R J 2014 Vortex flow during early and late left ventricular filling in normal subjects: quantitative characterization using retrospectively-gated 4D flow cardiovascular magnetic resonance and three-dimensional vortex core analysis *J. Cardiovasc. Magn. Reson.* **16** 78

Fadnes S, Nyrnes S A, Torp H and Lovstakken L 2014 Shunt flow evaluation in congenital heart disease based on two-dimensional speckle tracking *Ultrasound Med. Biol.* **40** 2379–91

Faurie J, Baudet M, Assi K C, Auger D, Gilbert G, Tournoux F and Garcia D 2017 Intracardiac vortex dynamics by high-frame-rate Doppler vortography—*in vivo* comparison with vector flow mapping and 4D flow MRI *IEEE Trans. Ultrason. Ferroelectr. Freq. Control* **64** 424–32

Garcia D *et al* 2010 Two-dimensional intraventricular flow mapping by digital processing conventional color-Doppler echocardiography images *IEEE Trans. Med. Imaging* **29** 1701–13

Gomez A, de Vecchi A, Jantsch M, Shi W, Pushparajah K, Simpson J M, Smith N P, Rueckert D, Schaeffter T and Penney G P 2015 4D Blood Flow Reconstruction over the entire ventricle from wall motion and blood velocity derived from ultrasound data *IEEE Trans. Med. Imaging* **34** 2298–308

Hansen P C 2000 The *L*-curve and its use in the numerical treatment of inverse problems *Computational Inverse Problems in Electrocardiology Advances in Computational Bioengineering* ed P Johnston (Ashurst: WIT Press) pp 119–42

Hansen P and O'Leary D 1993 The use of the L-curve in the regularization of discrete ill-posed problems *SIAM J. Sci. Comput.* **14** 1487–503

Hendabadi S, Bermejo J, Benito Y, Yotti R, Fernández-Avilés F, del Álamo J C and Shadden S C 2013 Topology of blood transport in the human left ventricle by novel processing of Doppler echocardiography *Ann. Biomed. Eng.* **41** 2603–16

Jang J, Ahn C Y, Jeon K, Heo J, Lee D, Joo C, Choi J and Seo J K 2015 A reconstruction method of blood flow velocity in left ventricle using color flow ultrasound *Comput. Math. Methods Med.* **2015** e108274

Jensen J A 1996 Color flow mapping using phase shift estimation *Estimation of Blood Velocities Using Ultrasound* (Cambridge: Cambridge University Press) pp 195–226

Jensen J A, Nikolov S, Yu A C H and Garcia D 2016 Ultrasound vector flow imaging: I: sequential systems *IEEE Trans. Ultrason. Ferroelectr. Freq. Control* **63** 1704–21

Kim H B, Hertzberg J R and Shandas R 2004 Echo PIV for flow field measurements in vivo *Biomed. Sci. Instrum.* **40** 357–63

Markl M, Schnell S, Wu C, Bollache E, Jarvis K, Barker A J, Robinson J D and Rigsby C K 2016 Advanced flow MRI: emerging techniques and applications *Clin. Radiol.* **71** 779–95

Mehregan F, Tournoux F, Muth S, Pibarot P, Rieu R, Cloutier G and Garcia D 2014 Doppler vortography: a color Doppler approach to quantification of intraventricular blood flow vortices *Ultrasound Med. Biol.* **40** 210–21

Muth S, Dort S, Sebag I A, Blais M-J and Garcia D 2011 Unsupervised dealiasing and denoising of color-Doppler data *Med. Image Anal.* **15** 577–88

Nogami Y, Ishizu T, Atsumi A, Yamamoto M, Kawamura R, Seo Y and Aonuma K 2013 Abnormal early diastolic intraventricular flow 'kinetic energy index' assessed by vector flow mapping in patients with elevated filling pressure *Eur. Heart J. Cardiovasc. Imaging* **14** 253–60

Pedrizzetti G, La Canna G, Alfieri O and Tonti G 2014 The vortex, an early predictor of cardiovascular outcome? *Nat. Rev. Cardiol.* **11** 545–53

Pedrizzetti G and Tonti G 2012 Method for transforming a Doppler velocity dataset into a velocity vector field *Patent No.* EP2514368 A1

Porée J, Posada D, Hodzic A, Tournoux F, Cloutier G and Garcia D 2016 High-frame-rate echocardiography using coherent compounding with Doppler-based motion-compensation *IEEE Trans. Med. Imaging* **35** 1647–57

Posada D, Porée J, Pellissier A, Chayer B, Tournoux F, Cloutier G and Garcia D 2016 Staggered multiple-PRF ultrafast color Doppler *IEEE Trans. Med. Imaging* **35** 1510–21

Provost J, Papadacci C, Arango J E, Imbault M, Fink M, Gennisson J-L, Tanter M and Pernot M 2014 3D ultrafast ultrasound imaging *in vivo Phys. Med. Biol.* **59** L1–3

Ro R, Halpern D, Sahn D J, Homel P, Arabadjian M, Lopresto C and Sherrid M V 2014 Vector flow mapping in obstructive hypertrophic cardiomyopathy to assess the relationship of early systolic left ventricular flow and the mitral valve *J. Am. Coll. Cardiol.* **64** 1984–95

Sengupta P P, Pedrizzetti G, Kilner P J, Kheradvar A, Ebbers T, Tonti G, Fraser A G and Narula J 2012 Emerging trends in CV flow visualization *JACC Cardiovasc. Imaging* **5** 305–16

Tanaka T, Asami R, Kawabata K, Itatani E K, Uejima T, Nishiyama T and Okada T 2015 Intracardiac VFM technique using diagnostic ultrasound system *Hitachi Rev.* **64** 489

Uejima T, Koike A, Sawada H, Aizawa T, Ohtsuki S, Tanaka M, Furukawa T and Fraser A G 2010 A new echocardiographic method for identifying vortex flow in the left ventricle: numerical validation *Ultrasound Med. Biol.* **36** 772–88

Weiss J 1991 The dynamics of enstrophy transfer in two-dimensional hydrodynamics *Phys. Nonlinear Phenom.* **48** 273–94

Intraventricular vector flow mapping (*i*VFM) –
a Doppler-based regularized problem with automatic model selection

K.C. Assi, E. Gay, C. Chnafa, S. Mendez, F. Nicoud, J.F.P.J. Abascal, P. Lantelme, F. Tournoux, D. Garcia

www.biomecardio.com; garcia.damien@gmail.com

The objective is to recover the intraventricular velocity vector field from a single Doppler field. We work in a regular polar grid whose center corresponds to the origin of the Doppler sector. The radial and angular coordinates of the velocity vector field $\vec{v}$ are noted $\{v_r, v_\theta\}$.

By convention, the Doppler velocities u_D are positive when blood flows towards the ultrasound probe. We note $v_D = -u_D$ to ensure sign compatibility between v_D and the radial components v_r of the estimated velocity field.

The cost function to be minimized is the following (see details in the main text):

$$J(\vec{v}) = \underbrace{\int_\Omega (v_r - v_D)^2}_{\substack{\text{fit to the} \\ \text{Doppler data}}}$$

$$+ \lambda_1 \underbrace{\int_\Omega (r\partial_r v_r + v_r + \partial_\theta v_\theta)^2}_{\substack{\text{physical} \\ \text{constraint}}}$$

$$+ \lambda_2 \underbrace{\int_{\partial\Omega} (\vec{v}\cdot\vec{n}|_{wall})^2}_{\substack{\text{boundary} \\ \text{conditions}}}$$

$$+ \lambda_3 \sum_{m\in\{r,\theta\}} \underbrace{\int_\Omega (r^2\partial_r^2 v_m)^2 + 2(r\partial_{r\theta}^2 v_m)^2 + (\partial_\theta^2 v_m)^2}_{\text{smoothness constraint}}$$

- • ∘ and ⊗ = Hadamard and Kronecker products, respectively

- $\mathbf{V_D}$ = matrix of size $(M \times N)$ contains the negative Doppler velocities.
- $\mathbf{V_r}$ and $\mathbf{V_\theta}$ = matrices of size $(M \times N)$ contain the radial and angular velocities
- $\mathbf{R}$ = matrix of size $(M \times N)$ contains the radial coordinates
- $\mathbf{N_r}$ and $\mathbf{N_\theta}$ = matrices of size $(M \times N)$ contain the radial and angular components of the unit vector normal to the left ventricular inner wall. $(\mathbf{N_r})_{k,l}$ and $(\mathbf{N_\theta})_{k,l} = 0$ if the element (k,l) is not on the edge of the left ventricular ROI (endocardium).
- We work with the elements inside and on edge of the region defined by the left ventricular cavity. This region is defined by the binary matrix $\mathbf{\Delta}$, with $(\mathbf{\Delta})_{k,l} = 1$ if the element (k,l) is inside or on edge of the ROI, $(\mathbf{\Delta})_{k,l} = 0$ otherwise.

- h_r and h_θ = radial and angular steps. They are constant since the polar grid is evenly-spaced.

The vectorized forms are:
- $v_r = \text{vec}(V_r)$, $v_\theta = \text{vec}(V_\theta)$ and $v_D = \text{vec}(V_D)$
- $n_r = \text{vec}(N_r)$, $n_\theta = \text{vec}(N_\theta)$
- $r = \text{vec}(R)$
- $\delta = \text{vec}(\Delta)$
- $r^{\circ 2} = r \circ r$

- I_p = identity matrix of size $(p \times p)$
- O_p = null matrix of size $(p \times p)$
- $\mathbb{I}_p$ = column vector of ones of size $(p \times 1)$

- $\dot{D}_p$ = 1st-order derivative operator matrix of size $(p \times p)$ =
$$\begin{bmatrix} -0.5 & 0.5 & & & & & \\ -0.5 & 0 & 0.5 & & & & \\ & -0.5 & 0 & 0.5 & & & \\ & & & \ddots & & & \\ & & & -0.5 & 0 & 0.5 & \\ & & & & -0.5 & 0 & 0.5 \\ & & & & & -0.5 & 0.5 \end{bmatrix}$$

- $\ddot{D}_p$ = 2nd-order derivative operator matrix of size $(p \times p)$ =
$$\begin{bmatrix} -1 & 1 & & & & \\ 1 & -2 & 1 & & & \\ & 1 & -2 & 1 & & \\ & & & \ddots & & \\ & & 1 & -2 & 1 & \\ & & & 1 & -2 & 1 \\ & & & & 1 & -1 \end{bmatrix}$$

- We note $\mathbf{v} = \begin{bmatrix} v_r^T & v_\theta^T \end{bmatrix}^T$ the column vector of size $(2MN \times 1)$, solution of the minimization problem.

Matrix formulation of the cost function

1. $v_r - v_D \xrightarrow{\substack{\text{matrix} \\ \text{form}}} V_r - V_D$

vectorization: $\text{vec}(V_r - V_D) = v_r - v_D = [I_{MN}, \quad O_{MN}]\, \mathbf{v} - v_D$

We note $Q_0 = [I_{MN} \quad O_{MN}]$
Q_0 is of size $(MN \times 2MN)$

2. $r\partial_r v_r + v_r + \partial_\theta v_\theta \xrightarrow{\overset{\text{matrix}}{\text{form}}} \boldsymbol{R} \circ \left(\frac{1}{h_r}\dot{\boldsymbol{D}}_{\boldsymbol{M}}\boldsymbol{V}_{\boldsymbol{r}}\right) + \boldsymbol{V}_{\boldsymbol{r}} + \frac{1}{h_\theta}\boldsymbol{V}_{\boldsymbol{\theta}}\dot{\boldsymbol{D}}_{\boldsymbol{N}}^{\mathrm{T}}$

vectorization:

$$\mathrm{vec}\left(\boldsymbol{R}\circ\left(\frac{1}{h_r}\dot{\boldsymbol{D}}_{\boldsymbol{M}}\boldsymbol{V}_{\boldsymbol{r}}\right) + \boldsymbol{V}_{\boldsymbol{r}} + \frac{1}{h_\theta}\boldsymbol{V}_{\boldsymbol{\theta}}\dot{\boldsymbol{D}}_{\boldsymbol{N}}^{\mathrm{T}}\right) = \frac{1}{h_r}\mathrm{vec}(\boldsymbol{R})\circ\mathrm{vec}(\dot{\boldsymbol{D}}_{\boldsymbol{M}}\boldsymbol{V}_{\boldsymbol{r}}) + \mathrm{vec}(\boldsymbol{V}_{\boldsymbol{r}}) + \frac{1}{h_\theta}\mathrm{vec}\left(\boldsymbol{V}_{\boldsymbol{\theta}}\dot{\boldsymbol{D}}_{\boldsymbol{N}}^{\mathrm{T}}\right)$$

$$= \frac{1}{h_r}\boldsymbol{r}\circ\left((\boldsymbol{I}_{\boldsymbol{N}}\otimes\dot{\boldsymbol{D}}_{\boldsymbol{M}})\boldsymbol{v}_{\boldsymbol{r}}\right) + \boldsymbol{v}_{\boldsymbol{r}} + \frac{1}{h_\theta}(\dot{\boldsymbol{D}}_{\boldsymbol{N}}\otimes\boldsymbol{I}_{\boldsymbol{M}})\,\boldsymbol{v}_{\boldsymbol{\theta}}$$

$$= \frac{1}{h_r}\left((\boldsymbol{r}\,\mathbb{I}_{\boldsymbol{MN}}^{\mathrm{T}})\circ(\boldsymbol{I}_{\boldsymbol{N}}\otimes\dot{\boldsymbol{D}}_{\boldsymbol{M}}) + \boldsymbol{I}_{\boldsymbol{MN}}\right)\boldsymbol{v}_{\boldsymbol{r}} + \frac{1}{h_\theta}(\dot{\boldsymbol{D}}_{\boldsymbol{N}}\otimes\boldsymbol{I}_{\boldsymbol{M}})\,\boldsymbol{v}_{\boldsymbol{\theta}}$$

$$= \left[\frac{1}{h_r}(\boldsymbol{r}\,\mathbb{I}_{\boldsymbol{MN}}^{\mathrm{T}})\circ(\boldsymbol{I}_{\boldsymbol{N}}\otimes\dot{\boldsymbol{D}}_{\boldsymbol{M}}) + \boldsymbol{I}_{\boldsymbol{MN}} , \quad \frac{1}{h_\theta}\dot{\boldsymbol{D}}_{\boldsymbol{N}}\otimes\boldsymbol{I}_{\boldsymbol{M}}\right]\boldsymbol{v}$$

We note $Q_1 = \left[\frac{1}{h_r}(\boldsymbol{r}\,\mathbb{I}_{\boldsymbol{MN}}^{\mathrm{T}})\circ(\boldsymbol{I}_{\boldsymbol{N}}\otimes\dot{\boldsymbol{D}}_{\boldsymbol{M}}) + \boldsymbol{I}_{\boldsymbol{MN}} , \quad \frac{1}{h_\theta}\dot{\boldsymbol{D}}_{\boldsymbol{N}}\otimes\boldsymbol{I}_{\boldsymbol{M}}\right]$

Q_1 is of size $(MN \times 2MN)$

3. $\vec{v}\cdot\vec{n}|_{wall} \xrightarrow{\overset{\text{matrix}}{\text{form}}} \boldsymbol{V}_{\boldsymbol{r}}\circ\boldsymbol{N}_{\boldsymbol{r}} + \boldsymbol{V}_{\boldsymbol{\theta}}\circ\boldsymbol{N}_{\boldsymbol{\theta}}$

vectorization: $\mathrm{vec}(\boldsymbol{V}_{\boldsymbol{r}}\circ\boldsymbol{N}_{\boldsymbol{r}} + \boldsymbol{V}_{\boldsymbol{\theta}}\circ\boldsymbol{N}_{\boldsymbol{\theta}}) = \boldsymbol{n}_{\boldsymbol{r}}\circ\boldsymbol{v}_{\boldsymbol{r}} + \boldsymbol{n}_{\boldsymbol{\theta}}\circ\boldsymbol{v}_{\boldsymbol{\theta}}$

We note $Q_2 = [\mathrm{diag}(\boldsymbol{n}_{\boldsymbol{r}}) \quad \mathrm{diag}(\boldsymbol{n}_{\boldsymbol{\theta}})]$

Q_2 is of size $(MN \times 2MN)$

4. $r^2\partial_r^2 v_r \xrightarrow{\overset{\text{matrix}}{\text{form}}} \boldsymbol{R}\circ\boldsymbol{R}\circ\left(\frac{1}{h_r^2}\ddot{\boldsymbol{D}}_{\boldsymbol{M}}\boldsymbol{V}_{\boldsymbol{r}}\right)$

vectorization: $\mathrm{vec}\left(\boldsymbol{R}\circ\boldsymbol{R}\circ\left(\frac{1}{h_r^2}\ddot{\boldsymbol{D}}_{\boldsymbol{M}}\boldsymbol{V}_{\boldsymbol{r}}\right)\right) =$

$$\frac{1}{h_r^2}\mathrm{vec}(\boldsymbol{R})\circ\mathrm{vec}(\boldsymbol{R})\circ\mathrm{vec}(\ddot{\boldsymbol{D}}_{\boldsymbol{M}}\boldsymbol{V}_{\boldsymbol{r}}) = \frac{1}{h_r^2}\boldsymbol{r}^{\circ 2}\circ\left((\boldsymbol{I}_{\boldsymbol{N}}\otimes\ddot{\boldsymbol{D}}_{\boldsymbol{M}})\boldsymbol{v}_{\boldsymbol{r}}\right) = \frac{1}{h_r^2}\left((\boldsymbol{r}^{\circ 2}\,\mathbb{I}_{\boldsymbol{MN}}^{\mathrm{T}})\circ(\boldsymbol{I}_{\boldsymbol{N}}\otimes\ddot{\boldsymbol{D}}_{\boldsymbol{M}})\right)\boldsymbol{v}_{\boldsymbol{r}}$$

$$\sqrt{2}r\partial_{r\theta}^2 v_r \xrightarrow{\overset{\text{matrix}}{\text{form}}} \sqrt{2}\boldsymbol{R}\circ\left(\frac{1}{h_r h_\theta}\dot{\boldsymbol{D}}_{\boldsymbol{M}}\boldsymbol{V}_{\boldsymbol{r}}\dot{\boldsymbol{D}}_{\boldsymbol{N}}^{\mathrm{T}}\right)$$

vectorization: $\mathrm{vec}\left(\sqrt{2}\boldsymbol{R}\circ\left(\frac{1}{h_r h_\theta}\dot{\boldsymbol{D}}_{\boldsymbol{M}}\boldsymbol{V}_{\boldsymbol{r}}\dot{\boldsymbol{D}}_{\boldsymbol{N}}^{\mathrm{T}}\right)\right) =$

$$\frac{\sqrt{2}}{h_r h_\theta}\mathrm{vec}(\boldsymbol{R})\circ\mathrm{vec}\left(\dot{\boldsymbol{D}}_{\boldsymbol{M}}\boldsymbol{V}_{\boldsymbol{r}}\dot{\boldsymbol{D}}_{\boldsymbol{N}}^{\mathrm{T}}\right) = \frac{\sqrt{2}}{h_r h_\theta}\boldsymbol{r}\circ\left((\dot{\boldsymbol{D}}_{\boldsymbol{N}}\otimes\dot{\boldsymbol{D}}_{\boldsymbol{M}})\boldsymbol{v}_{\boldsymbol{r}}\right) = \frac{\sqrt{2}}{h_r h_\theta}\left((\boldsymbol{r}\,\mathbb{I}_{\boldsymbol{MN}}^{\mathrm{T}})\circ(\dot{\boldsymbol{D}}_{\boldsymbol{N}}\otimes\dot{\boldsymbol{D}}_{\boldsymbol{M}})\right)\boldsymbol{v}_{\boldsymbol{r}}$$

$$\partial_\theta^2 v_r \xrightarrow{\overset{\text{matrix}}{\text{form}}} \frac{1}{h_\theta{}^2} V_r \ddot{D}_N{}^{\mathrm{T}}$$

vectorization: $\mathrm{vec}\left(\frac{1}{h_\theta{}^2} V_r \ddot{D}_N{}^{\mathrm{T}}\right) = \frac{1}{h_\theta{}^2}\left(\ddot{D}_N \otimes I_M\right) v_r$

idem for the terms including v_θ.

$$\text{We note } Q_3 = \begin{bmatrix} I_2 \otimes \frac{1}{h_r{}^2}\left(\left(r^{\circ 2}\, \mathbb{I}_{MN}{}^{\mathrm{T}}\right) \circ \left(I_N \otimes \ddot{D}_M\right)\right) \\ I_2 \otimes \frac{\sqrt{2}}{h_r h_\theta}\left(\left(r\, \mathbb{I}_{MN}{}^{\mathrm{T}}\right) \circ \left(\dot{D}_N \otimes \dot{D}_M\right)\right) \\ I_2 \otimes \frac{1}{h_\theta{}^2}\left(\ddot{D}_N \otimes I_M\right) \end{bmatrix}$$

Q_3 is of size $(6MN \times 2MN)$

➤ The cost function to be minimized can be written in a matrix form as follows:

$$J(\boldsymbol{v}) = (Q_0 \boldsymbol{v} - \boldsymbol{v_D})^{\mathrm{T}} (Q_0 \boldsymbol{v} - \boldsymbol{v_D}) + \sum_{k=1\ldots3} \lambda_k\, \boldsymbol{v}^{\mathrm{T}} Q_k^{\mathrm{T}} Q_k \boldsymbol{v}$$

➤ Minimizing this cost function provides the velocity field:

$$\boldsymbol{v}_{\mathrm{VFM}} = \arg\min_{\boldsymbol{v}} \left(J(\boldsymbol{v})\right) \implies Q_0^{\mathrm{T}}(Q_0 \boldsymbol{v} - \boldsymbol{v_D}) + \sum_{k=1\ldots3} \lambda_k\, Q_k^{\mathrm{T}} Q_k \boldsymbol{v} = 0$$

$$\implies \left(Q_0^{\mathrm{T}} Q_0 + \sum_{k=1\ldots3} \lambda_k\, Q_k^{\mathrm{T}} Q_k\right) \boldsymbol{v} = Q_0^{\mathrm{T}} \boldsymbol{v_D}$$

i.e. the linear system to be solved reads:
$$\boldsymbol{A}\,\boldsymbol{v} = \boldsymbol{b}$$

with

$$\boldsymbol{A} = Q_0^{\mathrm{T}} Q_0 + \sum_{k=1\ldots3} \lambda_k\, Q_k^{\mathrm{T}} Q_k = \begin{bmatrix} 1 & 0 \\ 0 & 0 \end{bmatrix} \otimes I_{MN} + \sum_{k=1\ldots3} \lambda_k\, Q_k^{\mathrm{T}} Q_k$$

$$\text{and } \boldsymbol{b} = Q_0^{\mathrm{T}} \boldsymbol{v_D} = \begin{bmatrix} 1 \\ 0 \end{bmatrix} \otimes \boldsymbol{v_D}$$

$\boldsymbol{A}$ is a sparse symmetric matrix of size $(2MN \times 2MN)$; $\boldsymbol{b}$ is a column vector of size $(2MN \times 1)$